J. Fluid Mech. (2020), *vol*. 900, A24. © The Author(s), 2020.
Published by Cambridge University Press
doi:10.1017/jfm.2020.526

Analytical model of nonlinear evolution of single-mode Rayleigh–Taylor instability in cylindrical geometry

Zhiye Zhao[1,2], Pei Wang[2], Nansheng Liu[1] and Xiyun Lu[1,3,†]

[1]Department of Modern Mechanics, University of Science and Technology of China, Hefei, Anhui 230026, PR China

[2]Institute of Applied Physics and Computational Mathematics, Beijing 10094, PR China

[3]State Key Laboratory of Fire Science, University of Science and Technology of China, Hefei, Anhui 230026, PR China

(Received 25 February 2020; revised 19 June 2020; accepted 23 June 2020)

We present an analytical model of nonlinear evolution of two-dimensional single-mode Rayleigh–Taylor instability (RTI) in cylindrical geometry at arbitrary Atwood number for the first time. Our model covers a full scenario of bubble evolution from the earlier exponential growth to the nonlinear regime with the bubbles growing in time as $\frac{1}{2}a_b t^2$ for cylindrical RTI, other than as $V_b t$ for planar RTI, where a_b and V_b are the bubble acceleration and velocity, respectively. It is found that from this model the saturating acceleration a_b is formulated as a simplified function of the external acceleration, Atwood number and number of perturbation waves. This model's predictions are in good agreement with data from direct numerical simulations.

Key words: buoyancy-driven instability, nonlinear instability

1. Introduction

Rayleigh–Taylor instability (RTI) occurs at a perturbed interface between two fluids when an external acceleration imposes points from the heavier to the lighter fluid (Rayleigh 1900; Taylor 1950). The interface evolves gradually to the spikes of the heavier fluid penetrating into the lighter fluid, and the bubbles of the lighter fluid rising into the heavier fluid. This instability plays an important role in inertial confinement fusion (Nuckolls *et al.* 1972; Bodner *et al.* 1998; Besnard 2007) and supernova explosions (Gamezo *et al.* 2003; Caproni *et al.* 2015). To predict accurately the growth rate of bubbles/spikes is of great significance in understanding the dynamics of unstable interfaces.

Great advancement has been achieved for the planar RTI in the form of elegant analytical solutions for the bubble evolution. Specifically, for the linear regime defined by a limit of small perturbation amplitudes, η_0 ($k\eta_0 \ll 1$, k is the perturbation wavenumber), the perturbation to an inviscid incompressible RTI has an exponential growth (Rayleigh 1900; Taylor 1950) $\eta_0(t) \sim \eta_0(0)e^{\gamma t}$ with a growth rate $\gamma = \sqrt{A_T kg}$, where A_T is

† Email address for correspondence: xlu@ustc.edu.cn

the Atwood number $A_T = (\rho_h - \rho_l)/(\rho_h + \rho_l)$, ρ_h and ρ_l are the heavier and lighter fluid density, g is the magnitude of external acceleration $\boldsymbol{g}$ and $\eta_0(0)$ is the initial amplitude. For the nonlinear regime, as the amplitude becomes large enough ($k\eta_0 \sim 1$), the perturbation grows into bubbles that have a linear-in-time amplitude growth (Layzer 1955; Mikaelian 1998; Zhang 1998; Goncharov 2002; Mikaelian 2003; Sohn 2003; Zhang & Guo 2016) $\eta_0 \sim V_b t$, where V_b is the bubble velocity. Such a transition is commonly referred to as a 'nonlinear saturation', in terms that the bubble velocity saturates at $\sqrt{2A_T/(1+A_T)(g/C_g k)}$ (Goncharov 2002; Mikaelian 2003; Sohn 2003), where $C_g = 3$ and 1 for the two- and three-dimensional planar geometries, respectively. Valuable physical insights have been obtained by extensive studies on the planar RTI (Zhou 2017*a*,*b*), for example, as to explore the effects of viscosity (Hu *et al.* 2019), vorticity (Bian *et al.* 2020) and compressibility (Wieland *et al.* 2019; Luo *et al.* 2020).

The RTI also occurs in the convergence geometry for some practical cases, such as inertial confinement fusion (Nuckolls *et al.* 1972; Bodner *et al.* 1998; Besnard 2007) and supernova explosions (Gamezo *et al.* 2003; Caproni *et al.* 2015). Actually, most effects on the RTI in convergence geometries can be captured by use of cylindrical geometry (Weir, Chandler & Goodwin 1998; Mikaelian 2005; Zhou 2017*b*; Zhao *et al.* 2018), which is a canonical convergence geometry. On the other hand, the cylindrical geometry has been usually employed in experiments, because the perturbation growth of the RTI in the cylindrical geometry can be conveniently measured by a direct line-of-sight diagnostic access along the axial direction (Hsing *et al.* 1997; Wang *et al.* 2013). Thus, the cylindrical geometry has been widely used to study the convergence effects on the RTI growth. Such virtues have stimulated a variety of research efforts on the cylindrical RTI, including experimental measurements (Hsing *et al.* 1997; Weir *et al.* 1998), theoretical analyses (Epstein 2004; Mikaelian 2005; Yu & Livescu 2008; Forbes 2011; Chambers & Forbes 2012; Wang *et al.* 2013; Guo *et al.* 2018; Zhao *et al.* 2018) and numerical simulations (Glimm, Grove & Zhang 1999; Chambers & Forbes 2012; Joggerst *et al.* 2014; Morgan & Greenough 2016).

The cylindrical geometry has a profound influence on the RTI growth which has an intriguing dependence on the direction of uniform external acceleration $\boldsymbol{g}$ (Yu & Livescu 2008; Wang *et al.* 2013; Guo *et al.* 2018). Different instability growth rates are found for the convergent ($\boldsymbol{g}$ acting radially inward) and divergent ($\boldsymbol{g}$ acting radially outward) cases (Yu & Livescu 2008). For inviscid incompressible fluids, the perturbation of the cylindrical RTI in the linear regime also takes an exponential growth (Wang *et al.* 2013; Guo *et al.* 2018), i.e. $\gamma = \sqrt{A_T n g/r_0}$ for either the convergent or divergent case, where n is the number of perturbation waves and r_0, the radius of the unperturbed interface. This behaviour is similar to the planar RTI. While bubbles/spikes get formed, the weakly nonlinear model (Wang *et al.* 2013) only depicts that the inward growth of bubbles is greater than the outward growth of spikes in the divergent case at small A_T. However, the underlying nonlinear mechanisms are still unclear for the cylindrical RTI. To the best of our knowledge, a theoretical model for the nonlinear evolution of cylindrical RTI has never been proposed for the understanding of the RTI dynamics under the cylindrical geometry effect.

The characteristics of the RTI may be related to the spatial dimension of fluid domain (e.g. Chertkov 2003; Boffetta & Mazzino 2017). Actually, some physical mechanisms are also consistent with each other in the two- and three-dimensional cases. Based on the analytical investigation (Goncharov 2002) and numerical simulation (Bian *et al.* 2020), the two- and three-dimensional bubble velocities saturate to constant values in the nonlinear stage for single-mode RTI. Therefore, the two-dimensional investigations are useful in understanding the physical mechanisms of the RTI (Zhang & Guo 2016; Hu *et al.* 2019;

Wieland *et al.* 2019; Luo *et al.* 2020). Moreover, the two-dimensional cylindrical geometry, or a circular region in polar coordinates, is usually used to investigate the convergence effects on the RTI (Weir *et al.* 1998; Mikaelian 2005; Zhou 2017*b*; Zhao *et al.* 2018).

In the present study, an analytical model of nonlinear evolution of two-dimensional single-mode RTI in cylindrical geometry has been derived for inviscid, irrotational and incompressible fluids, and verified via high-fidelity direct numerical simulation (DNS). The remainder of this paper is organized as follows. The DNS strategy for verifying the theoretical model is briefly described in § 2. The analytical model of nonlinear evolution of RTI in cylindrical geometry is given and the relevant results are discussed in § 3. Finally the concluding remarks are addressed in § 4.

2. Numerical simulations

2.1. *Governing equations*

DNS has been performed on the RTI of cylindrical geometry for verifying the theoretical model and analysing the relevant behaviours. Considering the RTI of cylindrical geometry described by the cylindrical coordinates (r, θ), the initial pressure p_I and density $\rho_I = (\rho_h + \rho_l)/2$ at the heavier/lighter fluid interface are chosen as the characteristic scales, where ρ_h and ρ_l are the heavier and lighter fluid density. Then the characteristic velocity and temperature are described as $U_I = \sqrt{p_I/\rho_I}$ and $T_I = p_I/(R\rho_I)$ with the perfect gas constant, R, respectively. The radius of the unperturbed interface, r_0, is used as the characteristic length. Thus, the non-dimensionalized governing equations are given as

$$\frac{\partial \rho}{\partial t} + \boldsymbol{\nabla} \cdot (\rho \boldsymbol{u}) = 0, \tag{2.1}$$

$$\frac{\partial (\rho \boldsymbol{u})}{\partial t} + \boldsymbol{\nabla} \cdot (\rho \boldsymbol{u}\boldsymbol{u}) = -\boldsymbol{\nabla} p + \frac{1}{Re}\boldsymbol{\nabla} \cdot \boldsymbol{\tau} - \frac{\rho}{Fr}\widehat{\boldsymbol{e}}_r, \tag{2.2}$$

$$\frac{\partial (\rho E)}{\partial t} + \boldsymbol{\nabla} \cdot [(\rho E + p)\boldsymbol{u}] = \frac{1}{Re}\boldsymbol{\nabla} \cdot (\boldsymbol{\tau} \cdot \boldsymbol{u}) + \frac{1}{RePr}\boldsymbol{\nabla} \cdot (\boldsymbol{\nabla} T) - \frac{\rho}{Fr}\boldsymbol{u} \cdot \widehat{\boldsymbol{e}}_r, \tag{2.3}$$

where t, ρ, $\boldsymbol{u} = [u_r, u_\theta]$, p, T and $E = T/(\Gamma - 1) + \boldsymbol{u} \cdot \boldsymbol{u}/2$ denote the time, density, velocity, pressure, temperature and total energy, respectively, where $\Gamma = 1.4$ is the specific heat ratio. Here, $\widehat{\boldsymbol{e}}_r$ is the unit vector in the radial direction. The stress tensor is obtained as

$$\boldsymbol{\tau} = 2\mu \boldsymbol{S} - \frac{2}{3}\mu(\boldsymbol{\nabla} \cdot \boldsymbol{u})\boldsymbol{\delta}, \tag{2.4}$$

where $\boldsymbol{S}$ is the strain-rate tensor, $\mu = T^{3/2}(1 + c)/(T + c)$ is the viscosity computed by the Sutherland law, with $c = 110/T_r$ and the reference temperature T_r and $\boldsymbol{\delta}$ is the unit tensor. The above governing equations are closed with the equation of state of ideal gas, i.e. $p = \rho T$.

The non-dimensional parameters in (2.1)–(2.3) are the Reynolds, Froude and Prandtl numbers defined, respectively, as

$$Re = \frac{\rho_I U_I r_0}{\mu_I}, \quad Fr = \frac{U_I^2}{r_0 g} \quad \text{and} \quad Pr = C_p \frac{\mu_I}{\kappa}, \tag{2.5a–c}$$

where g is the external acceleration, C_p the constant-pressure specific heat and κ the thermal conductivity.

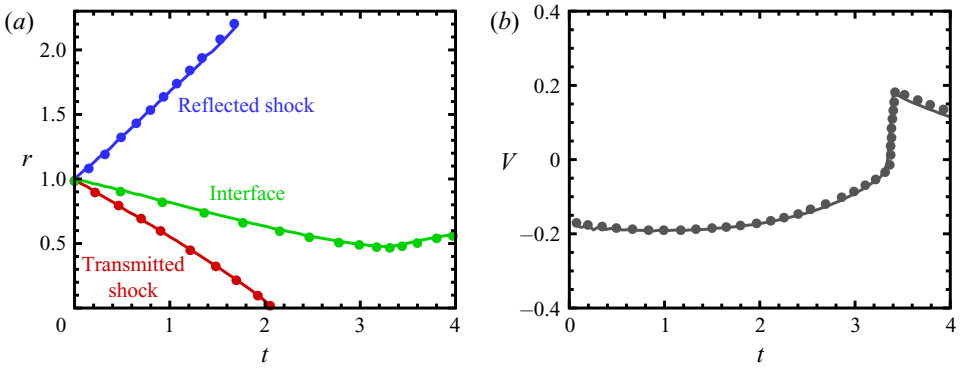

FIGURE 1. (*a*) Positions of the material interface, transmitted shock and reflected shock versus time. (*b*) Velocity of the material interface versus time. The lines represent the results of our DNS, and the circles represent those of Zhang & Graham (1998).

2.2. *Numerical method and validation*

The present DNS of cylindrical RTI is performed based on a numerical algorithm composed of high-order accuracy schemes to solve the compressible Navier–Stokes equations in cylindrical coordinates (Li *et al.* 2019). Specifically, the seventh-order finite difference weighted essentially non-oscillatory (WENO) scheme is implemented to discretize the convective terms (Jiang & Shu 1996) and the eighth-order central difference scheme to discretize the viscous terms in the governing equations (2.1)–(2.3). The time derivative is approximated by the standard third-order Runge–Kutta method.

To validate our DNS algorithm, we typically employ the multicomponent Riemann problem in cylindrical geometry (Zhang & Graham 1998), i.e. an incident circular shock colliding with a circular material interface. This problem also involves dynamical evolution of cylindrical interfaces, similar to the RTI problem considered here. However, it is much more complicated as the material interface evolves due to its interaction with moving shocks, and thus contains both density and pressure discontinuities. The test calculation is set following Zhang & Graham (1998), namely, an incident shock with shock Mach number 1.2 propagates inward from the air towards the SF_6 (sulphur hexafluoride). Figure 1(*a*) shows the positions of the material interface, transmitted shock and reflected shock, which agree well with those of Zhang & Graham (1998). The velocity of the material interface in figure 1(*b*) is also in good agreement with the data of Zhang & Graham (1998). The relevant extensive tests ensure that the present DNS is reliable for capturing interfacial dynamics.

2.3. *Problem statement and numerical results for cylindrical RTI*

To avoid the instability suppression due to background stratification, the uniform density field is initialized as $\rho_h = 1 + A_T$ and $\rho_l = 1 - A_T$ on each side of the interface (Bian *et al.* 2020), where the Atwood number $A_T = (\rho_h - \rho_l)/(\rho_h + \rho_l)$. The initial velocity field is set to be zero. The hydrostatic equilibrium requires that $\mathrm{d}p/\mathrm{d}r = -\rho_i/Fr (i = l, h)$ away from the interface, thus the pressure field can be determined by assuming $p = 1$ at the interface. The initial temperature field can be obtained by the equation of state. The interface at $r_0 = 1$ is perturbed by the cosine wave $\eta_0(0)\cos(n\theta)$, where $\eta_0(0)$ is the initial amplitude and n is the number of perturbation waves. The velocity, pressure and density at the far boundary are fixed at their initial values to ensure hydrostatic equilibrium (Hu *et al.* 2019).

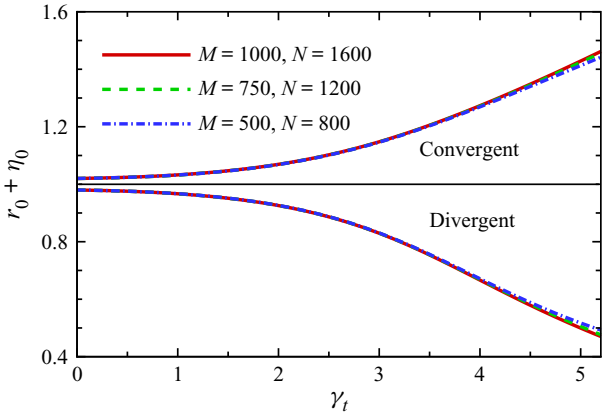

FIGURE 2. Location of the bubble tip for $A_T = 0.6$ and $n = 4$ with different grid resolutions.

Although a uniform density field is initialized to avoid the background stratification, the dynamic compressibility of flow should be noticed. Here, we present the relevant analysis. The reference Mach number, $Ma = u_\infty/c_\infty$, is used to consider the dynamic compressibility, where the reference velocity for single-mode RTI is $u_\infty = \sqrt{A_T g\lambda/(1 + A_T)}$ (Bian *et al.* 2020) with λ being the perturbation wavelength, and the reference sound speed is $c_\infty = \sqrt{\Gamma p_I/\rho_I}$. Thus, the reference Mach number reaches $Ma = \sqrt{A_T/(1 + A_T)(2\pi/nFr\Gamma)}$. In the present study, the Froude number is selected as $Fr = 10$ for the convergent case and as $Fr = -10$ for the divergent case, the Atwood number is $A_T = 0.3$ and 0.6, the numbers of perturbation waves are $n = 4$ and 8, the Prandtl number is $Pr = 0.72$ for air and the Reynolds number is $Re = 40\,000$. Based on these parameters, the typical case with $A_T = 0.6$ and $n = 4$ used in our simulations has the maximum reference Mach number 0.205. Therefore, we can reasonably determine that the compressibility effect on the RTI simulations is weak.

In the present simulation, to avoid a pole singularity at the centre of cylindrical coordinates, the inner boundary radius $r_{min} = 0.05$ has been used based on the previous treatment (e.g. Annamalai *et al.* 2014; Lombardini, Pullin & Meiron 2014). To verify that the spatial resolutions are enough to predict properly the RTI evolution, we present some typical results calculated by three sets of the grid resolution, i.e. $M = 500$, 750 and 1000 in the radial direction; $N = 800$, 1200 and 1600 in the circumferential direction, respectively. The radial grids are set as $r_{i+1} = r_i(1 + \Delta\theta)$, where r_i is the radial position of the ith grid and the width of uniform circumferential grids $\Delta\theta = 2\pi/N$. Figure 2 shows the location of the bubble tip with different grid resolutions for a typical case $A_T = 0.6$ and $n = 4$. The location of the bubble is determined as the point of the bubble tip with $\rho = \rho_I$. It is seen that the results collapse together for the different grid resolutions. To make the prediction accurate, the results given in the following were calculated by $M = 1000$ and $N = 1600$, which are enough to properly resolve the hydrodynamic scales.

The reliability of simulations for cylindrical RTI is also verified by comparing the positions of the bubble tips with the exponential growth (Wang *et al.* 2013; Guo *et al.* 2018) that $\eta_0 = \eta_0(0)\cosh(\gamma t)$ for inviscid incompressible RTI in the linear regime. As shown in figure 3, it is seen that the numerical simulation results are in good agreement with the linear theory, indicating that the simulation results are reliable and the effects of compressibility and viscosity can be reasonably ignored. When $\gamma t > 1.4$, the simulation results with $n = 8$ somewhat deviate from the linear theory, which is related to the fact that the RTI begins to enter the nonlinear stage.

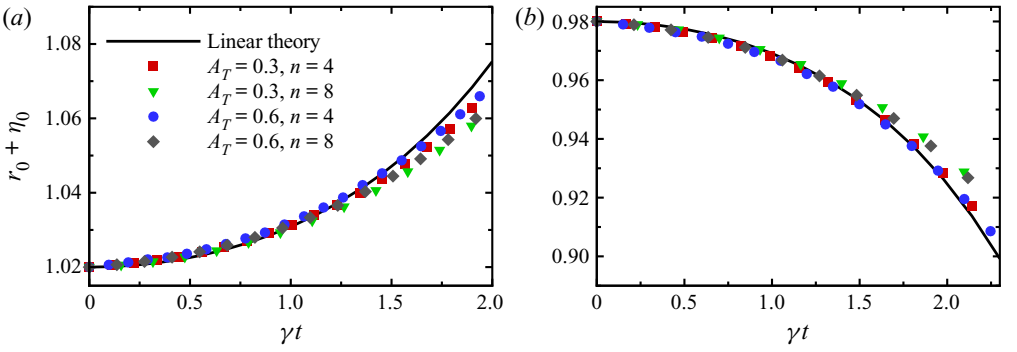

FIGURE 3. Comparisons of radial positions of bubble tips for the convergent (*a*) and divergent (*b*) cases with linear theory.

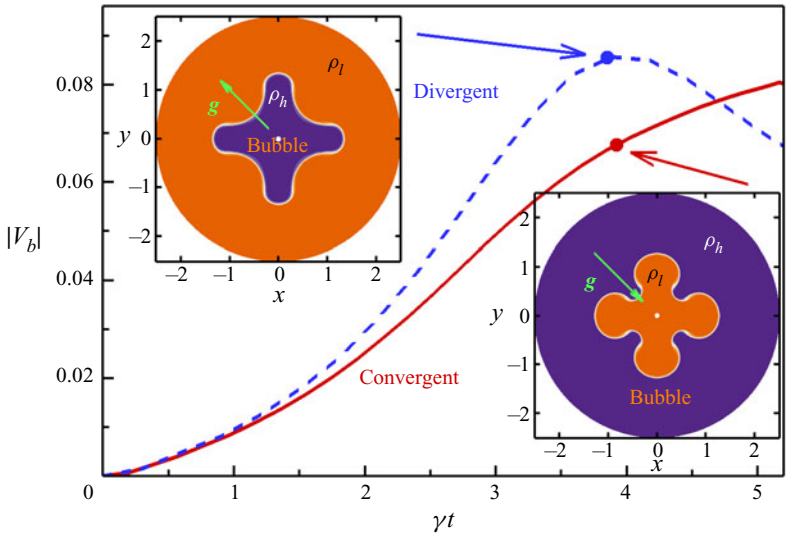

FIGURE 4. Bubble velocity growth of cylindrical RTI at $A_T = 0.6$ obtained by DNS.

Further, figure 4 shows our numerical results on the bubble velocity behaviours for the convergent and divergent cases in the nonlinear regime. The bubble velocity is determined at the point of the bubble tip with $\rho = \rho_l$. It is revealed that the bubble velocity of the divergent case when $\gamma t \leq 4.6$ prevails, and when $\gamma t > 4.6$ becomes overridden by that of the convergent case. Of particular interest, no evident saturation of bubble velocity is realized as in the planar RTI. Therefore, to understand the bubble dynamics under the cylindrical geometry effect, an analytical model for the nonlinear evolution of cylindrical RTI is presented as follows.

3. Analytical models

3.1. *Model of nonlinear bubble evolution*

We consider two inviscid, irrotational, incompressible fluids that have a cylindrical perturbed interface $r_l(\theta, t) = r_0 + \eta(\theta, t)$, where $\eta(\theta, t)$ is the perturbation displacement. The external acceleration is imposed as $\boldsymbol{g} = -g\widehat{\boldsymbol{e}}_r$ for the convergent case and as $\boldsymbol{g} = g\widehat{\boldsymbol{e}}_r$

for the divergent case. The velocity potentials of the lighter (φ_l) and heavier (φ_h) obey the Laplace equations

$$\Delta\varphi_l = \Delta\varphi_h = 0. \tag{3.1}$$

At the interface ($r = r_I$), the following kinematic and dynamic boundary conditions must be satisfied (Goncharov 2002; Wang *et al.* 2013):

$$\frac{\partial\eta}{\partial t} = \frac{\partial\varphi_l}{\partial r} - \frac{1}{r^2}\frac{\partial\eta}{\partial\theta}\frac{\partial\varphi_l}{\partial\theta} = \frac{\partial\varphi_h}{\partial r} - \frac{1}{r^2}\frac{\partial\eta}{\partial\theta}\frac{\partial\varphi_h}{\partial\theta}, \tag{3.2}$$

$$\rho_l\left(\frac{\partial\varphi_l}{\partial t} + \frac{|\nabla\varphi_l|^2}{2} + \Psi\right) - \rho_h\left(\frac{\partial\varphi_h}{\partial t} + \frac{|\nabla\varphi_h|^2}{2} + \Psi\right) = f(t), \tag{3.3}$$

where $f(t)$ is an arbitrary function of time, the potential of external force $\Psi = gr$ and $-gr$ for the convergent and divergent cases, respectively. In reality, (3.2) and (3.3) represent the continuity of the velocity component normal to the interface, and pressure at the interface. Following Layzer's treatment (Layzer 1955), we expand the perturbation of the bubble tip localized at the point $\{r, \theta\} = \{r_I(0, t), 0\}$ to the second order in θ, i.e. $\eta = \eta_0(t) + \eta_2(t)\theta^2$. A similar expanding procedure applied to (3.2) and (3.3) yields six equations for zero- to second-order of θ, which are well posed by six unknown functions of time. As three of these six functions have been given as $\eta_0(t)$, $\eta_2(t)$ and $f(t)$, the other three are required to be given by the velocity potentials. Inspired by Goncharov's model (Goncharov 2002), by solving the corresponding eigenvalue problem for the velocity potentials, the expressions of velocity potentials near the bubble tip are presumed as

$$\varphi_h = a_1(t)\cos(n\theta)\left(\frac{r}{r_0 + \eta_0(t)}\right)^{S_h n}, \tag{3.4}$$

$$\varphi_l = b_1(t)\cos(n\theta)\left(\frac{r}{r_0 + \eta_0(t)}\right)^{S_l n} + b_2(t)\ln\frac{r}{r_0 + \eta_0(t)}, \tag{3.5}$$

where $S_h = -1$ and $S_l = +1$ corresponding to the convergent case, and $S_h = +1$ and $S_l = -1$ to the divergent case. Note that φ_l is valid only near the bubble tip which cannot take the limit of $r \to 0$ and $r \to +\infty$ in (3.5). Thus only the first term of the Fourier series is kept in (3.4) and (3.5), which can obtain an excellent approximation at the bubble tip as verified by Goncharov (2002). Then the models for both the convergent and divergent cases are given as follows, respectively.

For the convergent case, using (3.4) and (3.5) and expanding (3.2) and (3.3) near the bubble tip, we have the following relations:

$$\dot\eta_2 = -\frac{(3n+1)\dot\eta_0}{r_0 + \eta_0}\eta_2 - \frac{n^2}{2}\dot\eta_0, \tag{3.6}$$

$$\frac{n^2 - 4A_T Hn - 12A_T H^2}{2(6H - n)(r_0 + \eta_0)}\frac{\mathrm{d}[(r_0 + \eta_0)\dot\eta_0]}{\mathrm{d}t} + \frac{A_T H\dot\eta_0^2}{r_0 + \eta_0} - \frac{(4A_T - 3)n^2 + 6(3A_T - 5)Hn + 36A_T H^2 + 12(A_T - 1)H}{2(6H - n)^2(r_0 + \eta_0)}n^2\dot\eta_0^2 = A_T gH, \tag{3.7}$$

where $H = \eta_2/(r_0 + \eta_0)$. Here, we assume the initial perturbation as $\eta_0(0)\cos(n\theta)$ and expand as $\eta_0(0)(1 - n^2\theta^2/2)$ at the bubble tip. Then, by integrating (3.6), it reads

$$H = \left[\frac{n^2}{6n+4} - \frac{n^2\eta_0(0)}{2(r_0+\eta_0(0))}\right]\left(\frac{r_0+\eta_0(0)}{r_0+\eta_0}\right)^{3n+2} - \frac{n^2}{6n+4}. \tag{3.8}$$

Further, by substituting (3.8) into (3.7) and integrating it, an analytic relation for the bubble amplitude can be obtained. In reality, such a relation is difficult to formulate explicitly because (3.7) is nonlinear. Thus the bubble amplitude can be determined by means of a numerical solution of (3.7).

Similarly, for the divergent case, an analytical model is given as

$$\begin{aligned} &-\frac{n^2 + 4A_THn - 12A_TH^2}{2(6H+n)(r_0+\eta_0)}\frac{\mathrm{d}[(r_0+\eta_0)\dot{\eta}_0]}{\mathrm{d}t} - \frac{A_TH\dot{\eta}_0^2}{r_0+\eta_0} \\ &\quad + \frac{(4A_T-3)n^2 - 6(3A_T-5)Hn + 36A_TH^2 + 12(A_T-1)H}{2(6H+n)^2(r_0+\eta_0)}n^2\dot{\eta}_0^2 = A_Tg H, \end{aligned} \tag{3.9}$$

$$H = \left[-\frac{n^2}{6n-4} - \frac{n^2\eta_0(0)}{2(r_0+\eta_0(0))}\right]\left(\frac{r_0+\eta_0}{r_0+\eta_0(0)}\right)^{3n-2} + \frac{n^2}{6n-4}. \tag{3.10}$$

To verify the above theoretical solutions, we employ our high-fidelity DNS on the evolution of the cylindrical RTI, especially in the nonlinear regime. Figure 5 shows the positions of the bubble tip for the convergent and divergent cases, where the Atwood number is chosen as $A_T = 0.3$ and 0.6, and the number of perturbation waves as $n = 4$ and 8 (coloured by red and blue, respectively) with an initial perturbation amplitude $\eta_0(0) = 0.02r_0$. It is identified that the results of the analytical models (3.7) and (3.9) are in good agreement with data from DNS. Further, it is found that the bubbles grow exponentially (see the black solid lines in figure 5) in the linear regime ($n\eta_0/r_0 \ll 1$), which is consistent with the linear theory (Wang *et al.* 2013), and a significant influence of the cylindrical geometry occurs in the nonlinear regime ($n\eta_0/r_0 > 1$).

3.2. *Model of nonlinear bubble saturation*

The effect of cylindrical geometry on the nonlinear evolution of RTI can be evidently revealed by the asymptotic solutions of (3.7) and (3.9). As shown in figure 5, taking the limit of $t \to \infty$, the asymptotic tendency is obtained as $(r_0 + \eta_0(0))/(r_0 + \eta_0) \to 0$ for the convergent case and $(r_0 + \eta_0)/(r_0 + \eta_0(0)) \to 0$ for the divergent case. Then substituting the above limits into (3.8) and (3.10), we have $H \to -n^2/(6n + 4)$ and $H \to n^2/(6n - 4)$ for the convergent and divergent cases, respectively. Finally, (3.7) and (3.9) are reduced as the following asymptotic ordinary differential equations:

$$\frac{1}{r_0+\eta_0}\frac{\mathrm{d}[(r_0+\eta_0)\dot{\eta}_0]}{\mathrm{d}t} + C\frac{\dot{\eta}_0^2}{r_0+\eta_0} = D, \tag{3.11}$$

$$\frac{1}{r_0+\eta_0}\frac{\mathrm{d}[(r_0+\eta_0)\dot{\eta}_0]}{\mathrm{d}t} + E\frac{\dot{\eta}_0^2}{r_0+\eta_0} = F, \tag{3.12}$$

where the constants $C - F$ can be obtained based on (3.7) and (3.9) and the asymptotic expression H. The solutions of (3.11) and (3.12) are derived as $\dot{\eta}_0/\sqrt{r_0+\eta_0} = \sqrt{2D/(3+2C)}$ and $\dot{\eta}_0/\sqrt{r_0+\eta_0} = -\sqrt{2F/(3+2E)}$, respectively.

Different from planar geometry, the bubble velocity $V_b = \dot{\eta}_0$ cannot saturate to a constant value in cylindrical geometry. Of special interest, $\dot{\eta}_0/\sqrt{r_0+\eta_0}$ approaches a

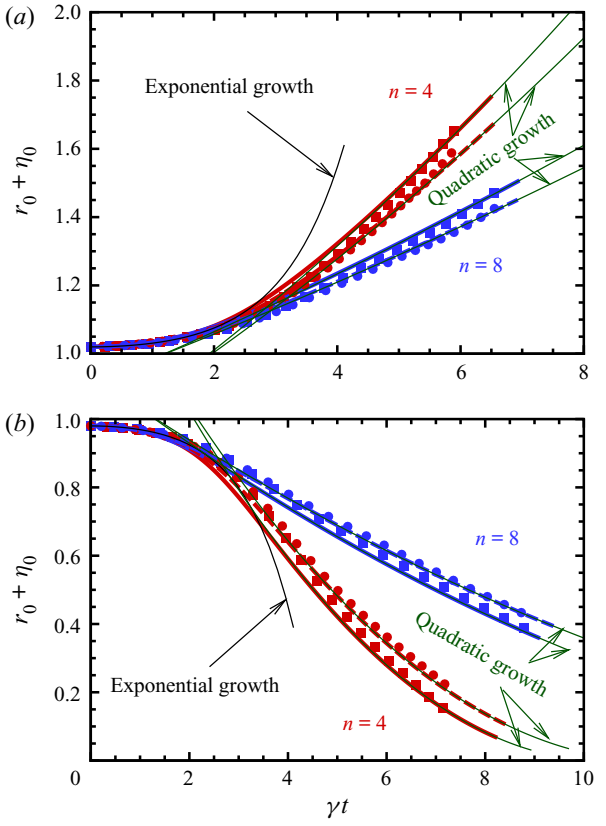

FIGURE 5. Radial positions of the bubble tip for the convergent (*a*) and divergent (*b*) cases at $A_T = 0.3$ (blue/red solid lines and squares) and $A_T = 0.6$ (blue/red dashed lines and circles) obtained by the analytical models (blue/red solid and dashed lines) and DNS (blue/red squares and circles). For comparison, the profiles are also plotted for the exponential growth (black solid thin line) with $\eta_0 = \eta_0(0)\cosh(\gamma t)$ in the linear regime given by Wang *et al.* (2013), and for quadratic-in-time growth (green solid thin lines) with $r_0 + \eta_0 \sim 1/2 a_b t^2$ in the nonlinear regime obtained by the present study.

constant value as $t \to \infty$, which is given as for the convergent and divergent cases, respectively,

$$\frac{\dot{\eta}_0}{\sqrt{r_0 + \eta_0}} \to \left(\frac{4n(3n+1)^2 A_T g}{54(A_T+1)n^4 + 9(15A_T+17)n^3 + 3(35A_T+53)n^2 + 24(A_T+3)n + 12} \right)^{\frac{1}{2}}, \tag{3.13}$$

$$\frac{\dot{\eta}_0}{\sqrt{r_0 + \eta_0}} \to -\left(\frac{4n(3n-1)^2 A_T g}{54(A_T+1)n^4 - 9(15A_T+17)n^3 + 3(35A_T+53)n^2 - 24(A_T+3)n + 12} \right)^{\frac{1}{2}}. \tag{3.14}$$

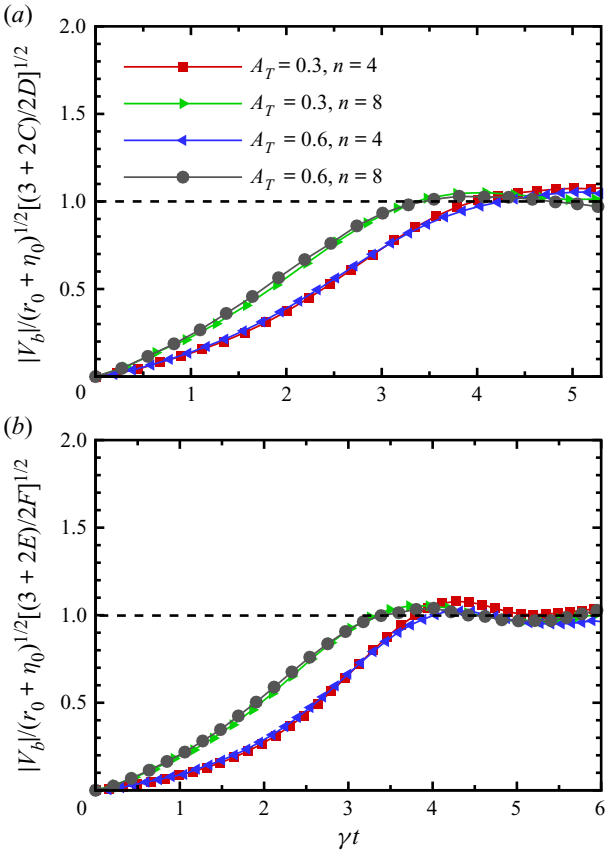

FIGURE 6. Normalized $|V_b|/\sqrt{r_0 + \eta_0}$ in convergent (a) and divergent (b) cases at $A_T = 0.3$ and 0.6 calculated by our DNS. Here, the dashed line of value 1 is plotted to illustrate the tendency of asymptotic analytical solution.

Further, the saturation of $V_b/\sqrt{r_0 + \eta_0}$ in the cylindrical RTI has been confirmed by our DNS results for $A_T = 0.3$ and 0.6 in figure 6. It is clearly identified that the normalized $|V_b|/\sqrt{r_0 + \eta_0}$ reaches approximately the expected quasi-steady value at $\gamma t \approx 4.0$ when the nonlinear bubble evolution is realized. The nonlinear bubble growth is quadratic-in-time, i.e. $r_0 + \eta_0 \sim 1/2 a_b t^2$ (see the green solid thin lines in figure 5), where the bubble acceleration is obtained analytically as $a_b = D/(3 + 2C)$ for the convergent case and as $a_b = F/(3 + 2E)$ for the divergent case. It reveals that the bubbles grow asymptotically with a motion of uniform acceleration in the nonlinear regime for the cylindrical RTI.

Based on the preceding analysis, when the cylindrical RTI grows from the linear into the nonlinear regime, the bubble evolution changes from the exponential to the quadratic-in-time growth. We could call such a transition 'nonlinear saturation' for the cylindrical RTI; it means that the bubble acceleration (or $V_b/\sqrt{r_0 + \eta_0}$) tends to be a constant value. As the bubble tip has $r_0 + \eta_0 \to \infty$ for the convergent case and $r_0 + \eta_0 \to 0$ for the divergent case, the bubble velocity is bound to have $V_b \to \infty$ and $V_b \to 0$ when the bubbles evolve in the nonlinear regime. Thus, it is rational that the bubble velocity of the divergent case is smaller than that of the convergent case at a certain moment, such as $\gamma t \geq 4.6$ in figure 4.

Furthermore, we can verify that the nonlinear saturation of cylindrical RTI (quadratic-in-time growth) could be reduced to that of planar RTI (linear-in-time growth), when the effect of cylindrical geometry becomes vanishingly small. The RTI in cylindrical geometry differs from that in plane geometry in two typical aspects. One is that the curvature effect $1/r_0$ occurs at the cylindrical interface, the other is that the external acceleration direction is not parallel, with the maximum angle $2\pi/n$ at single perturbation wave. Thus, the effect of cylindrical geometry will become negligibly weak as $r_0 \to \infty$ and $n \to \infty$. Further, the nonlinear saturation regime appears as $n\eta_0/r_0 \sim 1$, thus $r_0 \gg \eta_0$ lies in this regime as a result of the reduction of cylindrical geometry to a planar one. As $r_0 \gg \eta_0$ and $n \to \infty$, the right-hand sides of (3.13) and (3.14) are simplified as $\pm\sqrt{2A_T/(1+A_T)(g/3n)}$ as $n \to \infty$ and $\sqrt{r_0+\eta_0} \sim \sqrt{r_0}$ as $r_0 \gg \eta_0$. Then, (3.13) and (3.14) are reduced as $\dot{\eta}_0 \to \pm\sqrt{A_T g\lambda/(1+A_T)(1/3\pi)}$ with the perturbation wavelength $\lambda = 2\pi r_0/n$. The reduced bubble velocity is the same as that in the planar RTI (Goncharov 2002; Mikaelian 2003; Sohn 2003). This analysis also ensures that the nonlinear saturation models (3.13) and (3.14) are valid for the cylindrical RTI.

4. Concluding remarks

We have proposed an analytical model of nonlinear evolution for two-dimensional single-mode RTI in cylindrical geometry for inviscid, irrotational and incompressible fluids. This model reliably covers the full bubble evolution from the earlier exponential growth to the nonlinear regime saturating with a quadratic-in-time growth. The asymptotic solution of this model reveals that the nonlinear saturation is equivalent to a bubble growth of uniform acceleration. The saturating acceleration has been derived as a simplified function of the external acceleration, Atwood number and number of perturbation waves. This model can be reduced to that of the saturating bubble velocity of planar RTI as the cylindrical geometry effect vanishes. Further, this model's predictions are in good agreement with data from direction numerical simulations.

Although our analytical model is for inviscid single-mode RTI, we can take some inspiration from recent work (Xie *et al.* 2017; Kord & Capecelatro 2019) for the growth analysis of multimode RTI in cylindrical geometry by considering the effect of viscosity. The evolution of perturbation with short-wavelength mode is dominated by diffusion and its RTI growth will be suppressed due to the effect of viscosity. Hence, there exist optimal perturbations that the growth of multimode RTI in cylindrical geometry may be suppressed, which is worth being investigated. In addition, we are aware of the limitations of this analytical model based on the two-dimensional assumption; nevertheless, we feel that the results obtained from this model will be helpful in a physical understanding of the mechanisms of the RTI in cylindrical geometry.

Acknowledgements

The authors are very grateful to Professor R. Yan at USTC for helpful discussions. This work was supported by the Natural Science Foundation of China (no. 11621202) and the Science Challenge Project (no. TZ2016001).

REFERENCES

ANNAMALAI, S., PARMAR, M. K., LING, Y. & BALACHANDAR, S. 2014 Nonlinear Rayleigh–Taylor instability of a cylindrical interface in explosion flows. *Trans. ASME: J. Fluids Engng* **136** (6), 060910.

BESNARD, D. 2007 The megajoule laser program-ignition at hand. *Eur. Phys. J.* D **44**, 207–213.

BIAN, X., ALUIE, H., ZHAO, D.-X., ZHANG, H.-S. & LIVESCU, D. 2020 Revisiting the late-time growth of single-mode Rayleigh–Taylor instability and the role of vorticity. *Physica* D **403**, 132250.

BODNER, S. E., COLOMBANT, D. G., GARDNER, J. H., LEHMBERG, R. H., OBENSCHAIN, S. P., PHILLIPS, L., SCHMITT, A. J., SETHIAN, J. D., MCCRORY, R. L., SEKA, W. & OTHERS 1998 Direct-drive laser fusion: status and prospects. *Phys. Plasmas* **5**, 1901–1918.

BOFFETTA, G. & MAZZINO, A. 2017 Incompressible Rayleigh–Taylor turbulence. *Annu. Rev. Fluid Mech.* **49**, 119–143.

CAPRONI, A., LANFRANCHI, G. A., DA SILVA, A. L. & FALCETA-GONÇALVES, D. 2015 Three-dimensional hydrodynamical simulations of the supernovae-driven gas loss in the dwarf spheroidal galaxy URSA minor. *Astrophys. J.* **805**, 109–120.

CHAMBERS, K. & FORBES, L. K. 2012 The cylindrical magnetic Rayleigh–Taylor instability for viscous fluids. *Phys. Plasmas* **19** (10), 102111.

CHERTKOV, M. 2003 Phenomenology of Rayleigh–Taylor turbulence. *Phys. Rev. Lett.* **91** (11), 115001.

EPSTEIN, R. 2004 On the Bell–Plesset effects: the effects of uniform compression and geometrical convergence on the classical Rayleigh–Taylor instability. *Phys. Plasmas* **11** (11), 5114–5124.

FORBES, L. K. 2011 A cylindrical Rayleigh–Taylor instability: radial outflow from pipes or stars. *J. Engng Maths* **70** (1-3), 205–224.

GAMEZO, V. N., KHOKHLOV, A. M., ORAN, E. S., CHTCHELKANOVA, A. Y. & ROSENBERG, R. O. 2003 Thermonuclear supernovae: simulations of the deflagration stage and their implications. *Science* **299** (5603), 77–81.

GLIMM, J., GROVE, J. & ZHANG, Y.-M. 1999 Numerical calculation of Rayleigh–Taylor and Richtmyer–Meshkov instabilities for three dimensional axi-symmetric flows in cylindrical and spherical geometries. Preprint, SUNY at Stony Brook.

GONCHAROV, V. N. 2002 Analytical model of nonlinear, single-mode, classical Rayleigh–Taylor instability at arbitrary Atwood numbers. *Phys. Rev. Lett.* **88** (13), 134502.

GUO, H.-Y., WANG, L.-F., YE, W.-H., WU, J.-F. & ZHANG, W.-Y. 2018 Weakly nonlinear Rayleigh–Taylor instability in cylindrically convergent geometry. *Chin. Phys. Lett.* **35** (5), 055201.

HSING, W. W., BARNES, C. W., BECK, J. B., HOFFMAN, N. M., GALMICHE, D., RICHARD, A., EDWARDS, J., GRAHAM, P., ROTHMAN, S. & THOMAS, B. 1997 Rayleigh–Taylor instability evolution in ablatively driven cylindrical implosions. *Phys. Plasmas* **4** (5), 1832–1840.

HU, Z.-X., ZHANG, Y.-S., TIAN, B.-L., HE, Z.-W. & LI, L. 2019 Effect of viscosity on two-dimensional single-mode Rayleigh–Taylor instability during and after the reacceleration stage. *Phys. Fluids* **31** (10), 104108.

JIANG, G.-S. & SHU, C.-W. 1996 Efficient implementation of weighted ENO schemes. *J. Comput. Phys.* **126**, 202–228.

JOGGERST, C. C., NELSON, A., WOODWARD, P., LOVEKIN, C., MASSER, T., FRYER, C. L., RAMAPRABHU, P., FRANCOIS, M. & ROCKEFELLER, G. 2014 Cross-code comparisons of mixing during the implosion of dense cylindrical and spherical shells. *J. Comput. Phys.* **275**, 154–173.

KORD, A. & CAPECELATRO, J. 2019 Optimal perturbations for controlling the growth of a Rayleigh–Taylor instability. *J. Fluid Mech.* **876**, 150–185.

LAYZER, D. 1955 On the instability of superposed fluids in a gravitational field. *Astrophys. J.* **122**, 1–12.

LI, H.-F., HE, Z.-W., ZHANG, Y.-S. & TIAN, B.-L. 2019 On the role of rarefaction/compression waves in Richtmyer–Meshkov instability with reshock. *Phys. Fluids* **31** (5), 054102.

LOMBARDINI, M., PULLIN, D. I. & MEIRON, D. I. 2014 Turbulent mixing driven by spherical implosions. Part 1. Flow description and mixing-layer growth. *J. Fluid Mech.* **748**, 85–112.

LUO, T.-F., WANG, J.-C., XIE, C.-Y., WAN, M.-P. & CHEN, S.-Y. 2020 Effects of compressibility and Atwood number on the single-mode Rayleigh–Taylor instability. *Phys. Fluids* **32** (1), 012110.

MIKAELIAN, K. O. 1998 Analytic approach to nonlinear Rayleigh–Taylor and Richtmyer–Meshkov instabilities. *Phys. Rev. Lett.* **80** (3), 508–511.

MIKAELIAN, K. O. 2003 Explicit expressions for the evolution of single-mode Rayleigh–Taylor and Richtmyer–Meshkov instabilities at arbitrary Atwood numbers. *Phys. Rev.* E **67** (2), 026319.

MIKAELIAN, K. O. 2005 Rayleigh–Taylor and Richtmyer–Meshkov instabilities and mixing in stratified cylindrical shells. *Phys. Fluids* **17** (9), 094105.

MORGAN, B. E. & GREENOUGH, J. A. 2016 Large-eddy and unsteady RANS simulations of a shock-accelerated heavy gas cylinder. *Shock Waves* **26** (4), 355–383.

NUCKOLLS, J., WOOD, L., THIESSEN, A. & ZIMMERMAN, G. 1972 Laser compression of matter to super-high densities: thermonuclear (CTR) applications. *Nature* **239** (5368), 139–142.

RAYLEIGH, LORD 1900 Investigation of the character of the equilibrium of an incompressible heavy fluid of variable density. *Scientific Papers* 200–207, vol. II. Cambridge University Press.

SOHN, S.-I. 2003 Simple potential-flow model of Rayleigh–Taylor and Richtmyer–Meshkov instabilities for all density ratios. *Phys. Rev.* E **67** (2), 026301.

TAYLOR, G. I. 1950 The instability of liquid surfaces when accelerated in a direction perpendicular to their planes. I. *Proc. R. Soc. Lond.* A **201** (1065), 192–196.

WANG, L.-F., WU, J.-F., YE, W.-H., ZHANG, W.-Y. & HE, X.-T. 2013 Weakly nonlinear incompressible Rayleigh–Taylor instability growth at cylindrically convergent interfaces. *Phys. Plasmas* **20** (4), 042708.

WEIR, S. T., CHANDLER, E. A. & GOODWIN, B. T. 1998 Rayleigh–Taylor instability experiments examining feedthrough growth in an incompressible, convergent geometry. *Phys. Rev. Lett.* **80** (17), 3763–3766.

WIELAND, S. A., HAMLINGTON, P. E., RECKINGER, S. J. & LIVESCU, D. 2019 Effects of isothermal stratification strength on vorticity dynamics for single-mode compressible Rayleigh–Taylor instability. *Phys. Rev. Fluids* **4** (9), 093905.

XIE, C.-Y., TAO, J.-J., SUN, Z.-L. & LI, J. 2017 Retarding viscous Rayleigh–Taylor mixing by an optimized additional mode. *Phys. Rev.* E **95** (2), 023109.

YU, H.-D. & LIVESCU, D. 2008 Rayleigh–Taylor instability in cylindrical geometry with compressible fluids. *Phys. Fluids* **20** (10), 104103.

ZHANG, Q. 1998 Analytical solutions of layzer-type approach to unstable interfacial fluid mixing. *Phys. Rev. Lett.* **81** (16), 3391–3394.

ZHANG, Q. & GRAHAM, M. J. 1998 A numerical study of Richtmyer–Meshkov instability driven by cylindrical shocks. *Phys. Fluids* **10** (4), 974–992.

ZHANG, Q. & GUO, W.-X. 2016 Universality of finger growth in two-dimensional Rayleigh–Taylor and Richtmyer–Meshkov instabilities with all density ratios. *J. Fluid Mech.* **786**, 47–61.

ZHAO, K.-G., XUE, C., WANG, L.-F., YE, W.-H., WU, J.-F., DING, Y.-K., ZHANG, W.-Y. & HE, X.-T. 2018 Thin shell model for the nonlinear fluid instability of cylindrical shells. *Phys. Plasmas* **25** (9), 092703.

ZHOU, Y. 2017*a* Rayleigh–Taylor and Richtmyer–Meshkov instability induced flow, turbulence, and mixing. I. *Phys. Rep.* **720**, 1–136.

ZHOU, Y. 2017*b* Rayleigh–Taylor and Richtmyer–Meshkov instability induced flow, turbulence, and mixing. II. *Phys. Rep.* **723**, 1–160.